

Phase transitions and molecular dynamics of n-hexadecanol confined in silicon nanochannels

R. Berwanger¹, A. Henschel², K. Knorr², P. Huber², and R. Pelster¹

Universität des Saarlandes, ¹FR 7.2 Experimentalphysik & ²FR 7.3 Technische Physik,
66041 Saarbrücken, Germany

We present a combined x-ray diffraction and infrared spectroscopy study on the phase behavior and molecular dynamics of n-hexadecanol in its bulk state and confined in an array of aligned nanochannels of 8 nm diameter in mesoporous silicon. Under confinement the transition temperatures between the liquid, the rotator R_{II} and the crystalline C phase are lowered by approximately 20 K. While bulk n-hexadecanol exhibits at low temperatures a polycrystalline mixture of orthorhombic β - and monoclinic γ -forms, geometrical confinement favors the more simple β -form: only crystallites are formed, where the chain axis are parallel to the layer normal. However, the γ -form, in which the chain axis are tilted with respect to the layer normal, is entirely suppressed. The β -crystallites form bi-layers, that are not randomly orientated in the pores. The molecules are arranged with their long axis perpendicular to the long channel axis. With regard to the molecular dynamics, we were able to show that confinement does not affect the inner-molecular dynamics of the CH_2 scissor vibration and to evaluate the inter-molecular force constants in the C phase.

PACS numbers: 64.70.Nd, 61.46.Hk, 81.07.-b, 61.43.Gt

I. INTRODUCTION

The physical properties of condensed matter spatially confined in pores or channels of a few nanometer in diameter can differ markedly from the behavior in the bulk state. In particular, phase transitions can be entirely suppressed or significantly altered in comparison to their bulk counterparts^{1,2,3,4}. Also the dynamics of condensed matter confined in mesopores, most prominently in the vicinity of glass transitions^{5,6,7,8,9,10,11,12,13,14}, can be affected markedly.

Intimately related to these changes in the phase transition phenomenology the architectural principles of molecular solids can substantially differ in the spatially confined state from the bulk state. This depends, however, sensitively on the complexity of the building blocks. For simple van-der-Waals systems, such as Ar and N_2 , a remarkable robustness of the bulk structures has been found for the solid state under confinement^{15,16,17}. By contrast, the structural properties of pore fillings built out of more complex building blocks, such as linear hydrocarbons^{18,19,20,21,22} or liquid crystals^{23,24} are very susceptible to confinement on the meso- and nanoscale. For example, a quenching of the lamellar ordering of molecular crystals of n-alkanes has been observed in tortuous silica mesopores of Vycor²⁵. However, in tubular channels of mesoporous silicon this building principle of hydrocarbon molecular crystals survives, albeit a peculiar texture has been observed for the pore confined solids¹⁹: The long axes of the molecules and thus the stacking direction of the lamellae are oriented perpendicular to the long axis of the pores.

Here we present an experimental study on a medium-length, linear alcohol $\text{C}_{16}\text{H}_{33}\text{OH}$, a representative of the 1-alcohol series, imbibed in mesoporous silicon. We explore the phase behavior of the confined alcohol by a com-

bination of x-ray diffraction and infrared spectroscopy measurements. As we shall demonstrate, we profit in those experiments both from the parallel alignment of the silicon channels and from the transparency of the silicon host in the infrared region.

II. EXPERIMENTAL

The porous silicon samples used in this study were prepared by electrochemical etching of a heavily p-doped (100) silicon wafer¹ with a current density of $13 \frac{\text{mA}}{\text{cm}^2}$ in a solution composed of HF, ethanol and H_2O (1:3:1 per volume)^{26,27,28}. These conditions led to a parallel arrangement of non-interconnected channels oriented with their long axes along the $\langle 100 \rangle$ crystallographic direction of silicon, which coincides with the normal of the wafer surface. After the porous layer had reached the desired thickness of 70 microns, the anodization current was increased by a factor of ten with the result that the porous layer was released from the bulk wafer underneath. Using nitrogen sorption isotherms at $T = 77 \text{ K}$, we determined a porosity of 60% and a mean channel diameter of 8 nm. The single crystalline character of the matrix was checked by x-ray diffraction. Transmission electron micrographs of channel cross sections indicate polygonal, rough channel perimeters rather than circular, smooth circumferences²⁹.

The matrix both for the infrared spectroscopy and the x-ray measurements were filled completely via capillary action (spontaneous imbibition) with liquefied

¹ producer: SiMat, Landsberg, Germany; specific conductivity: $\rho = 0.01 - 0.025 \Omega\text{cm}$.

$C_{16}H_{33}OH$ ³⁰. Bulk excess material at the surface was removed by paper tissues.

Infrared spectra in a range of wavenumbers $\bar{\nu}$ from 4000 to 800 cm^{-1} with a resolution of 1 cm^{-1} were measured with a Fourier Transform Spectrometer (FTIR Perkin Elmer System 2000). This range corresponds to frequencies from $3 \cdot 10^{13}$ Hz to $1.2 \cdot 10^{14}$ Hz (wavelengths from 10 μm to 2.5 μm). For both the bulk material and the filled porous samples the same sample holder was used, i. e. a copper cell with two transparent KBr windows. In the confinement experiments the long channel axes were oriented parallel to the beam axis, i. e. perpendicular to the electric field vector. The sample holder was placed into a cryostat (a closed cycle refrigerator CTI cryogenics, Model 22) allowing us to vary the temperature from 50 to 340 K. The temperature was controlled with a LakeShore 340 temperature controller with a precision of ± 0.25 K. All IR-spectra that we show in the following were measured during cooling (**typical cooling rates were of the order of 0.5 K/min**). Heating scans show the same behavior except for the transition temperatures, which are some degrees higher (see below).

For the x-ray measurements the sample was mounted on a frame in a sample cell consisting of a Peltier cooled base plate and a Be cap. The cell was filled with He gas for better thermal contact. The Be cap sits in a vacuum chamber, the outer jacket of which has Mylar windows allowing the passage of the x-rays over a wide range of scattering angles θ within the scattering plane (see Fig. 1). But the set-up allowed practically no tilt with respect to the scattering plane. The temperature was controlled by a LakeShore 330 over an accessible range from 245 K up to 370 K. The measurements were carried out on a two-circle x-ray diffractometer with graphite monochromatized CuK_{α} radiation emanating from a rotating anode. The porous sheet was mounted perpendicular to the scattering plane. The two angles that could be varied were the detector angle 2θ and the rotation angle ω about the normal of the scattering plane. The samples were studied as a function of temperature by performing several Φ -scans. In this paper we concentrate on radial 2θ - ω -Scans in reflection geometry, i.e. along q_p with $\Phi=0^\circ$, and in transmission geometry, i.e. along q_s with $\Phi=90^\circ$ (see Fig. 1).

A. Structure of bulk n-hexadecanol

n-Hexadecanol, $C_{16}H_{33}OH$, is an almost rod-like molecule with a length of 22 Å and a width of 4 Å. The C-atoms of the backbone are in an all-trans-configuration so that they are located in a plane²⁵.

At low temperatures n-alcohols form bi-layered crystals in two possible modifications: the so-called γ -form, i. e. a monoclinic structure as sketched in Fig. 2 (C_{2h}^6 —

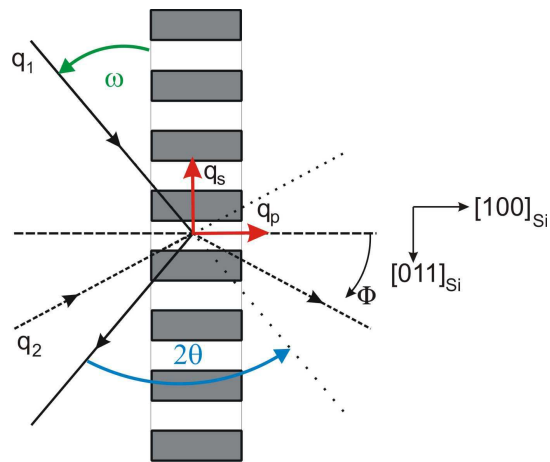


FIG. 1: (Color online) The angular variable Φ ($\Phi = \omega - \theta$ with $\Phi = 0^\circ$ for scans along q_p and $\Phi = 90^\circ$ for scans along q_s) is indicated. Also shown are the incoming and outgoing x-ray beam for scans along q_p (solid lines: wave vector component parallel to the pore axis, this means reflection geometry), and along q_s (dashed lines: wave vector component perpendicular to the pore axis; this is transmission geometry). For scans along q_p , the detector angle 2θ and the rotation angle ω are represented.

$A2/a$ ^{31,32}), or the so-called β -form, i. e. an orthorhombic structure as sketched in Fig. 3³³. In the γ -form, the molecules include an angle of 122° with the layer plane. Within the layers, they are close-packed in a quasi-hexagonal 2D array, described by the rectangular in-plane lattice parameters a and b (according to Ref.³² $a = 7.42$ Å and $b = 4.93$ Å holds, so that $a/b = 1.5$). There are two different alternating orientations for the C-C-plane of the backbone leading to a herringbone structure (see Fig. 2b). The β -form exhibits an identical orientational order of the backbone, but the molecules' axes remain perpendicular to the layers as sketched in Fig. 3³³. In addition, gauche- and trans-conformation of the CO-bond alternate with molecules in this phase, while they are in an all-trans configuration in the γ -form. In general, the γ -form dominates at low temperatures for the even alcohols, while the β -form is more frequent in odd n-alcohols^{33,34}. For n-hexadecanol both the orthorhombic β -form³³ and the monoclinic γ -form^{31,32} are reported. Depending on the preparation conditions it is possible to obtain a polycrystalline mixture of the monoclinic γ - and the orthorhombic β -form³⁴.

Upon heating, the crystalline phase undergoes a transition into a so-called Rotator-(II)-phase R_{II} , which is schematically depicted in Fig. 4². This phase has a hexagonal in-plane arrangement with the c -direction perpendicular to the cell base. The hexagonal arrangement

² For several alkanes, there also exists a Rotator-(I)-Phase R_I , where the molecules switch between two equal positions.

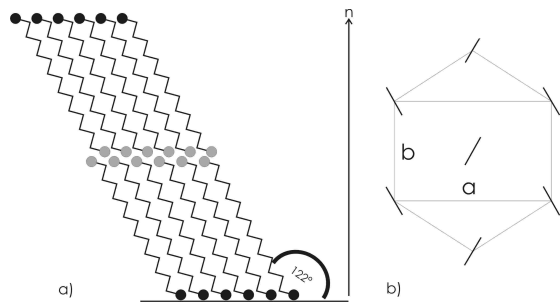


FIG. 2: γ -form of the crystalline low temperature phase of bulk $C_{16}H_{33}OH$ ($T \leq 310$ K). The structure is monoclinic. The left sketch shows the orientation of the molecules with respect to the layer normal n , the right sketch the in-plane arrangement, i. e. a projection of the backbones into the a - b -plane. Compare with the β -form sketched in Fig. 3

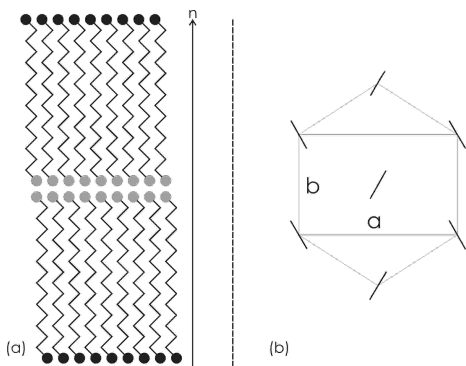


FIG. 3: β -form of the crystalline low temperature phase of $C_{16}H_{33}OH$. In contrast to the γ -form (see Fig. 2a), the long chain axes are not tilted but parallel to the layer normal n , i. e. the structure is orthorhombic. Bulk $C_{16}H_{33}OH$ can exhibit a polycrystalline mixture of γ - and β -form (see Sec. II A). Confinement into nanopores leads to the β -form (see below, Sec. III A).

can be indexed with an orthorhombic cell with a ratio of rectangular basal lattice parameters of $a/b = \sqrt{3}$ ³⁵. On a microscopic level the change in the center of mass lattice from the low-temperature crystalline phase to the rotator phase can be attributed to the onset of hindered rotations of the molecules about their long axes between six equivalent positions (the stars in Fig. 4b). Further heating above 322 K leads to the liquid state³⁵.

III. RESULTS

A. Structure of confined n-hexadecanol

We have determined structures, phase sequences and transition temperatures of n - $C_{16}H_{33}OH$ confined in mesoporous silicon by x-ray diffractometry. The upper panel in Fig. 5 shows diffraction patterns along q_p at se-

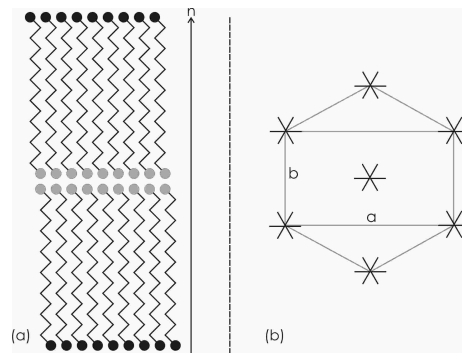


FIG. 4: Structure of bulk n -hexadecanol in the Rotator-(II)-phase (for $310 \leq T \leq 322$ K), a hexagonal arrangement. The right picture shows the perfect hexagonal lattice in the a - b -plane. Confined $C_{16}H_{33}OH$ exhibits the same structure in its rotator phase, but in a different temperature range (see below, Table II).

lected temperatures while cooling. The appearance of a broad Bragg peak at $2\theta \simeq 21^\circ$ indicates solidification. Its position is compatible with the leading hexagonal in-plane reflection of the R_{II} phase. Upon further cooling a second peak at $2\theta \simeq 24^\circ$ shows up. This change in the diffraction pattern indicates an uniaxial deformation of the hexagonal lattice. Both reflections can be mapped on a 2D rectangular mesh characteristic of an uniaxially deformed hexagonal cell. The overall resulting pattern is, however, incompatible with the monoclinic structure of the low temperature bulk crystalline phase.

Additionally to the q_p -scans, we performed also scans for a variety of additional orientations of the scattering vector with regard to the long axis of the channels. These patterns differ markedly, which is indicative of a strong texture of the pore confined crystallized alcohol. It is no powder in the crystallographic sense. In particular, there are strong in-plane reflections and no layering reflections for scans along q_p , while the q_s -scans for the same sample show at least very weak reflections characteristic of a bilayer stacking and only very weak leading in-plane reflections (see Fig. 5). An analysis of the width of the layering reflections yields a coherence length of $7 (\pm 1.5)$ nm.

As discussed in more detail in Refs.¹⁹ and³⁶, the overall picture which emerges from these results can be summed up as follows: the alcohol molecules form orthorhombic structures with a bilayer-stacking direction along the c -direction. Within the bilayers (the a - b -plane), the molecules' backbones are untilted with regard to the stacking direction and the backbones are orientationally either fully ordered (in a herringbone fashion) or partially ordered, as known from the R_I phase of n -alkanes. The superlattice reflection characteristic of the full, herringbone type orientational ordering has been searched for and could weakly be detected at low temperatures. The degree of uniaxial deformation of the hexagonal center of mass cell, quantified by the deviation of the ratio a/b from its value in the hexagonal phase ($\sqrt{3}$), also in-

dicates a full orientational ordered state (see Table I,³²). Thus, the diffraction data are compatible with the bulk β modification discussed above. This conclusion is also supported by an analysis of the infrared spectroscopy data sets presented below.

More importantly, the peculiar dependency of the diffraction patterns on the orientation of the q-vector with regard to the silicon host indicate that the bi-layer stacking direction is perpendicular to the long axis of the channels and, consequently, that the long axis of the molecules is oriented perpendicular to the long axis of the channels (see Fig. 6). At first glance, this finding may appear somewhat counter-intuitive. Albeit it can be understood as resulting from the crystallization process in a strongly anisotropic, capillary-like confined liquid^{19,37}. It is a well established principle in single crystal growth that in narrow capillaries the fastest growing crystallization direction prevails over other directions and propagates along the long axes of capillaries³⁸. For layered molecular crystals of rod-like building blocks this direction is an in-plane direction, which is perpendicular to the long axis of the rods. If this direction is aligned parallel to the silicon nanochannels due to the crystallization process, it dictates a perpendicular arrangement of the molecules' long axes with regard to the long channel axis, in agreement with the diffraction results presented here.

	bulk		confinement	
	cryst.	R_{II}	cryst.	
a [Å]	7.42	8.35	7.33	
b [Å]	4.93	4.82	5.04	
a/b	1.51	$\sqrt{3}$	1.45	
d [Å]	8.91	9.64	8.90	

TABLE I: Lattice parameters a and b of bulk and confined $C_{16}H_{33}OH$ and the diagonal $d = \sqrt{a^2 + b^2}$ of the subcell (see Fig. 14). The confined data result from our x-ray measurements and the bulk data are taken from the literature³².

The temperature dependent diffraction study allows us to gain additional information on the relative stability of the different nanochannel confined phases. In Table II we display the phase transition temperatures of confined $C_{16}H_{33}OH$ as inferred from the appearance or disappearance of characteristic Bragg peaks. There is a hysteresis between heating and cooling for both the fluid- R_{II} - and the R_{II} -C-transition (8 K and 3 K, respectively). Compared to the bulk data (see also Tab. II), the transition temperatures of pore confined $C_{16}H_{33}OH$ are lowered. On cooling, the lowering is of the order of $\Delta T = 18$ K for the fluid- R_{II} -transition and $\Delta T = 26$ K for the R_{II} -C-transition. This observation is analogous to phase transitions shifts reported for other pore condensates^{2,3}.

Furthermore, the temperature range of the confined R_{II} phase, 14 K upon cooling and 19 K upon heating, is larger than that of the bulk material (12 K). Obviously, confinement stabilizes the orientational disordered R_{II}

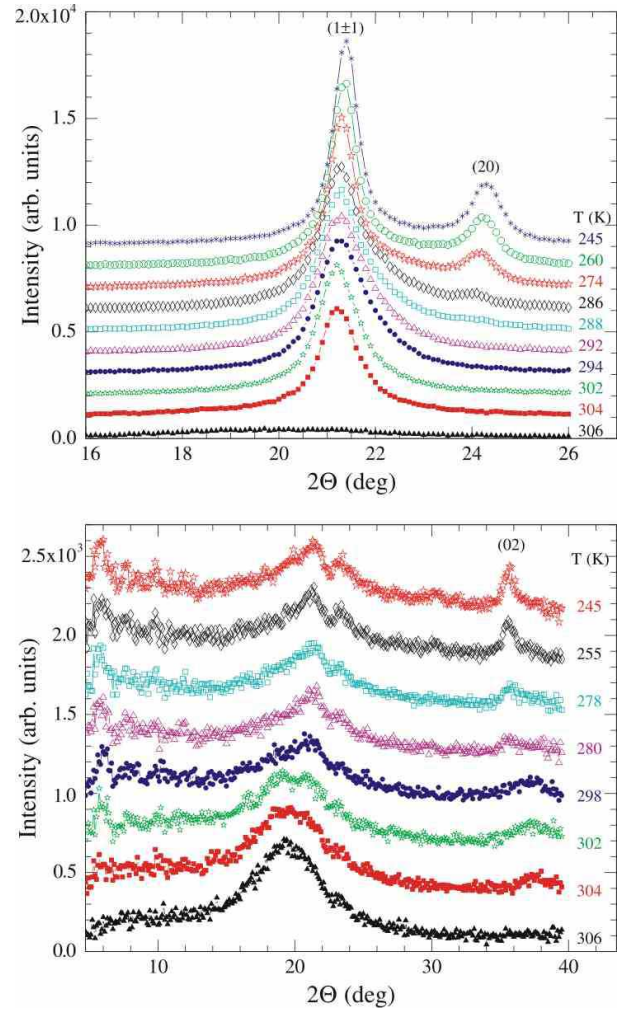


FIG. 5: (Color online) Upper panel: Diffraction pattern of q_{\parallel} -scans of pore confined $C_{16}H_{33}OH$ while cooling at selected temperatures. Lower panel: Diffraction pattern of q_{\perp} -scans at selected temperatures while cooling. The leading in-plane reflections are barely visible. Moreover, at lower angles ($2\theta \leq 10$) there are very weak and diffuse layering reflections.

phase, similarly as has been found for n-alkanes¹⁹ and for other orientational disordered, plastic phases under spatial confinement⁴.

Since the pores were completely filled at higher temperatures, when hexadecanol is in its liquid state, the pore filling at low temperatures does not consist only of bi-layer crystals: the change of volume at the R_{II} -C phase transition is about 10% (see Fig. 7), so that there are voids and/or molecules that are not part of a bi-layer crystal. However, our experiments do not give us information about their spatial arrangement.

	fluid - R_{II}	R_{II} - C	fluid - R_{II}	R_{II} - C
confined (cooling)	304	291		
confined (heating)	312	293		
bulk			322	310

TABLE II: Transition temperatures as determined by x-ray experiments of confined and bulk $C_{16}H_{33}OH$ ³⁵. They agree with those inferred from IR - measurements (CH_2 -scissoring vibration), see Figs. 10 and 11.

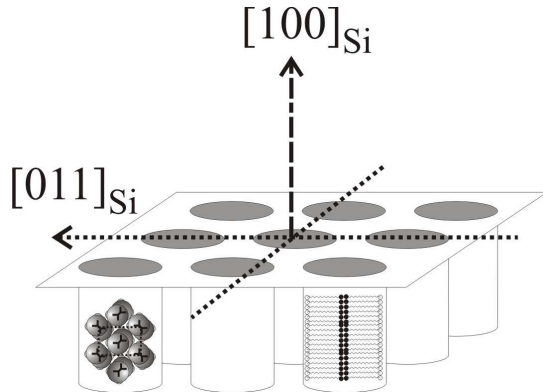


FIG. 6: Sketch of the orientation of pore condensed $C_{16}H_{33}OH$ in the porous sheet. Left pore: view on the rectangular in-plane arrangement of the molecules. Right pore: bi-layered crystal; the long molecule axis are oriented perpendicular to the pore axes. At maximum two bi-layers fit into a pore.

B. Molecular dynamics

The dynamics of bulk- $C_{16}H_{33}OH$ has already been investigated in IR-measurements in the past^{31,33}. In order to show later on how the molecular dynamics is affected by spatial confinement on the nm-scale, we display some of our bulk spectra in the following.

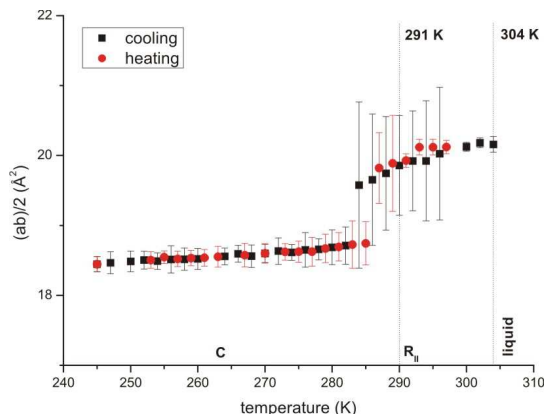


FIG. 7: (color online). Temperature dependence of the area per molecule A for $C_{16}H_{33}OH$ confined in porous silicon.

Here we focus on two characteristic vibrations, the OH-stretching and the CH_2 -scissoring vibration.

Figs. 8a) and 9a) show the bulk spectra of the OH-stretching-band in the respective phases (compare with Figs. 2-4). In the liquid state (above 322 K) the peak maximum is located at about 3345 cm^{-1} . A decrease of temperature below 321 K yields a shift of the peak position to about 3325 cm^{-1} indicating the molecular rearrangement in the R_{II} phase. A further decrease of temperature below 310 K results in a splitting into two peaks at approximately 3310 cm^{-1} and 3220 cm^{-1} . Confined $C_{16}H_{33}OH$ shows a different behavior. There is only one peak in the whole temperature range, the position of which changes reflecting the transition between liquid phase and R_{II} phase as well as between R_{II} phase and C phase (see Figs. 8b and 9b).

The fact that the OH-band of bulk $C_{16}H_{33}OH$ splits at low temperatures while no splitting is observed under confinement confirms the structural differences already observed in the x-ray experiment. For example, Tasumi et. al have studied bulk alcohols $C_nH_{2n+1}OH$ from $n = 11 - 37$ using infrared spectroscopy³³, Ventòla et al. alcohols with $n = 17 - 20$ ³⁴. Those alcohols showing at low temperatures (C phase) the monoclinic γ -form, such as $C_{16}H_{33}OH$, exhibit the splitting of the OH-band, while those that take the orthorhombic β -form show a single peak. This is due to differences in the spatial arrangement of the hydrogen bonds as well as in the distances of neighboring O-atoms: in the crystalline γ -form, where the molecule axis are tilted (see Fig. 2), the molecules show an all trans conformation, and the intra-layer O-distance ($\simeq 2.74\text{ Å}$) differs from the inter-layer O-distance ($\simeq 2.69\text{ Å}$). However, in the orthorhombic β -form (Fig. 3) trans- and gauche-molecules alternate and the intra-layer O-distance (2.73 Å) nearly equals the inter-layer O-distance (2.72 Å), so that the splitting is suppressed³³. Therefore, the observed OH-band splitting for bulk $C_{16}H_{33}OH$ shows the presence of the γ -form. Either the whole bulk material exhibits the γ -form or there is a mixture of γ - and β -crystallites. The latter case is frequently observed^{33,34}: in fact, in the range of wavenumbers from 1150 cm^{-1} to 950 cm^{-1} , where C-C stretching vibrations are visible, we see indications for a superposition of both forms (not shown). On the other hand, pore confined $C_{16}H_{33}OH$ shows no OH-band-splitting at low temperatures. This reflects that the molecular arrangement doesn't transform in the monoclinic γ -form but remains in an orthorhombic structure, i. e. only the β -form is present (compare Figs. 2 and 3). This result is in agreement with the x-ray data presented above. **Upon cooling, both the bulk and the confined hexadecanol pass from an hexagonal R_{II} - phase into a crystalline phase. The bulk material undergoes a stronger structural change, i. e. there is a mixture of the orthorhombic β - and the monoclinic γ -form. The latter one is suppressed under confinement, so that only the β -form remains, which**

is quite similar to the hexagonal structure of the R_{II} -phase: the fact that the crystallites have to fit into nanopores of irregular shape might favor the geometrically more simple β -form^{3,39}(see Fig. 6).

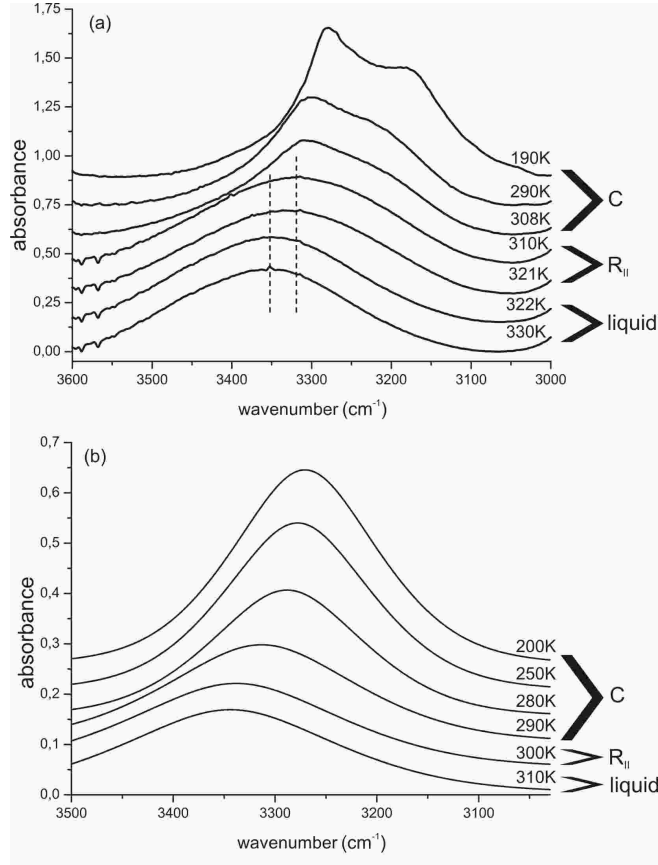


FIG. 8: (a) IR spectrum in the OH - stretching range for bulk $C_{16}H_{33}OH$. At lower temperatures the peak shifts to lower wavenumbers and then splits into two peaks. (b) Spectrum for confined $C_{16}H_{33}OH$, where no splitting is visible.

Now let us turn towards the scissor-vibration of the CH_2 groups (bending mode) that will give us information about inner-molecular and inter-molecular force constants. The spectra are shown in Fig. 10. At first, we want to discuss the bulk material. At high temperatures (liquid state) a superposition of two peaks at 1467 cm^{-1} and 1460 cm^{-1} is observed. In the intermediate temperature range (R_{II} phase; see Fig. 4) the intensity of the peak labeled "1" increases strongly. At low temperatures (C phase; see Fig. 2) this band splits up into two peaks. The latter transition can be clearly seen in Figs. 11a) and 12a), where we display the peak positions and intensities as a function of temperature. The results are similar to those obtained for the bulk state of n-paraffines, that apart from the missing OH-group are similar in their structure, i. e. that have the same CH_2 -backbone⁴⁰. In IR-spectra only one CH_2 -scissoring-band is observed at high temperatures, i. e. intra-molecular interactions of the CH_2 -groups are too small to lead to a series of distinct

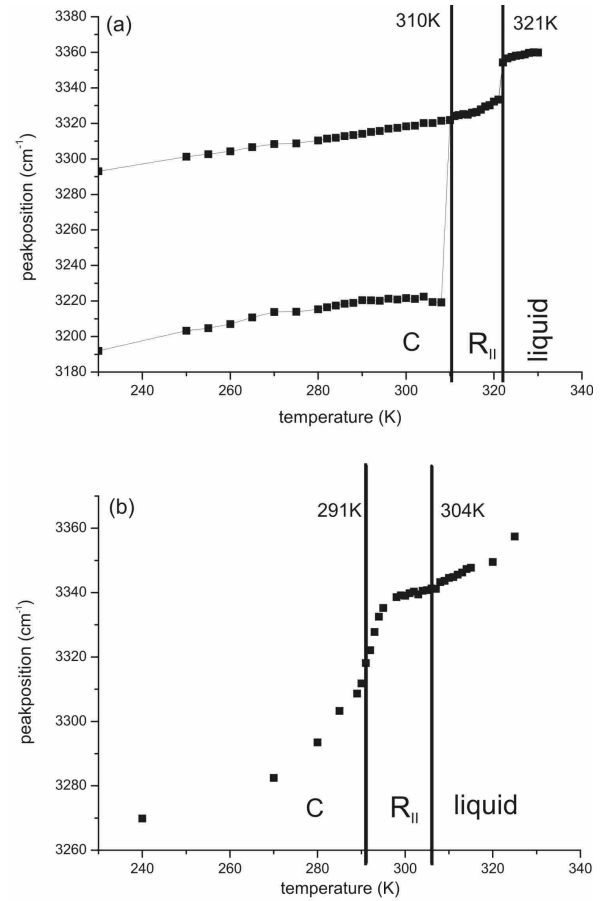


FIG. 9: (a) Wavenumber $\omega/2\pi c$ of the OH - stretching peak vs temperature for bulk $C_{16}H_{33}OH$ [compare with Fig. 8a)]. Three different phases are visible: a) above 321 K, b) from 310 to 321 K, where the peak position appears at lower wavenumbers and c) below 310 K where the peak splits up into two peaks. (b) Wavenumber of the OH - stretching peak for confined $C_{16}H_{33}OH$ (compare with Fig. 8b). The transition between the C and the R_{II} phase seems to be smeared in a range around $T = 291 \pm 5\text{ K}$. The R_{II} -liquid transition does not affect the OH-stretching.

peaks. The band splitting at low temperatures has been attributed to inter-molecular interactions (see Ref.⁴⁰ and text below).

Qualitatively, a behavior similar to that of the bulk state is observed for confined $C_{16}H_{33}OH$ (see Fig. 10b). In the high-temperature liquid phase two overlapping peaks are visible. The stronger one, i. e. that at higher wavenumbers, undergoes an increase in intensity at about 304 K (see Fig. 12b), indicating the transition from the liquid phase to the R_{II} phase, while the secondary peak at lower wavenumbers gets weaker and finally disappears. At the second transition temperature of $T = 291\text{ K}$ the remaining strong peak splits (see also Fig. 11b). The separation is not as distinct as for bulk material. These transition temperatures, $T = 304\text{ K}$ and $T = 291\text{ K}$ (see Figs. 11b and 12b), agree well with

those obtained via x-ray measurements (compare with Table II).

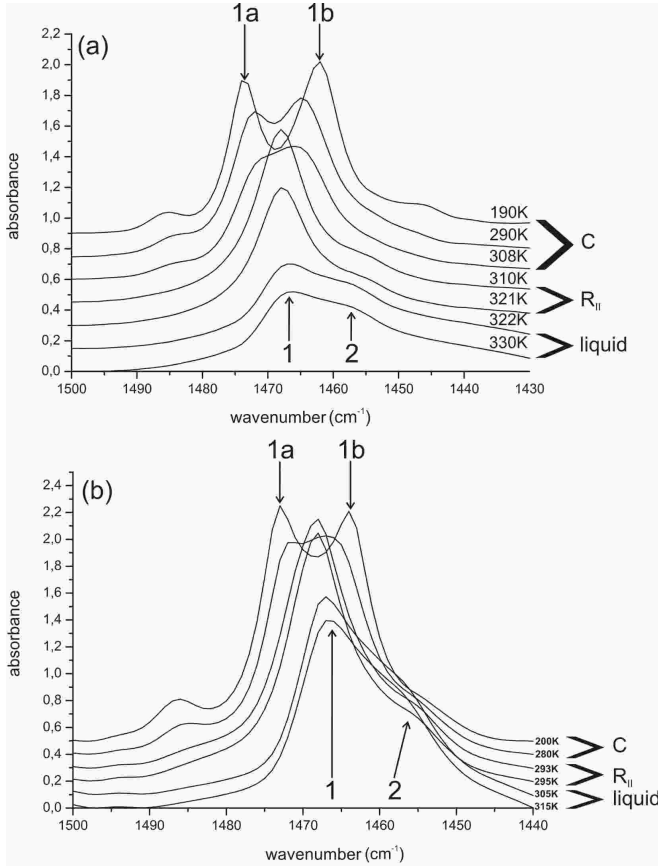


FIG. 10: (a) IR spectrum showing the CH₂ scissor-vibration for bulk C₁₆H₃₃OH at various temperatures. (b) IR spectrum showing the CH₂ scissor-vibration of C₁₆H₃₃OH confined in mesoporous Si at various temperatures.

In the following we want to analyze the dynamics of the CH₂-groups in order to check whether it is affected by the geometric confinement, e. g. by an interaction with the pore surfaces, by the limited number of neighboring molecules (finite-size-effects) or by structural changes. In a first approximation we can assume that it is not affected by the stretching of the OH - groups. On the one hand, there is the scissor vibration, where the angle α between the two CH-bonds oscillates around its equilibrium value $\alpha = 109.47^\circ$ (see Fig. 13). In addition, symmetric and asymmetric stretching vibrations of the CH-bonds are observable (for the values see Table III). Let f_α and f_d denote the respective force constants. These can be calculated from the measured vibration frequencies using Eqs. (26)-(28) (see Appendix A; the difference in calculating f_α via Eq. (27) or Eq. (28) is below 3.5% confirming that the intermolecular coupling terms can be neglected). Table III shows the results for the liquid and the R_{II} phase. Neither the phase transition liquid \rightarrow R_{II} nor geometrical

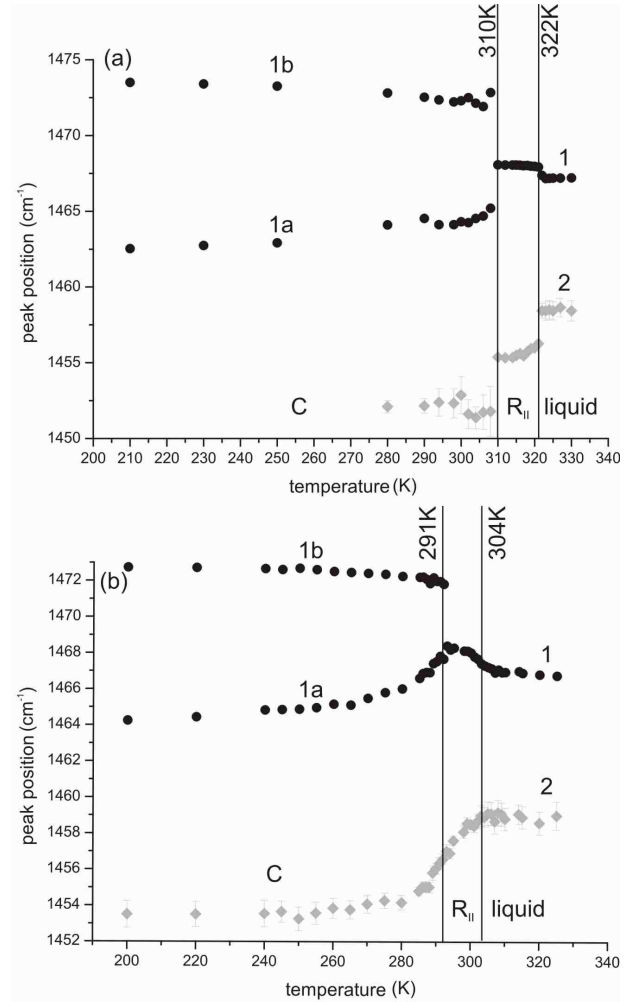


FIG. 11: Wavenumber of the CH - scissor peak vs temperature for (a) bulk C₁₆H₃₃OH and (b) confined C₁₆H₃₃OH (the peak labels refer to Fig. 10).

confinement does markedly affect the innermolecular constants.

In the R_{II} phase the molecules rotate about their long axis, so that the primitive cell consists of only one molecule per layer (see Fig. 4). Therefore, no splitting is observed. But in the C phase (below 310 K for bulk and below 291 K for confined C₁₆H₃₃OH), where the molecules are arranged in a herringbone structure, there are two molecules per layer in the primitive cell. So the symmetry of the arrangement allows a splitting of the scissoring band and obviously the molecular interactions are sufficiently strong that we are able to observe a double peak (see above, Figs. 10 and 11). The strength of interaction depends on the distances between neighboring H-atoms of adjacent chains and can be analyzed using a formalism developed by Snyder (see Ref.⁴⁰ and Appendix B). In Fig. 14 we have sketched the orthorhombic lattice of the crystalline C₁₆H₃₃OH subcell (a view on the a-b-plane perpendicular to the molecules axis). In what follows we restrict ourselves to this β -

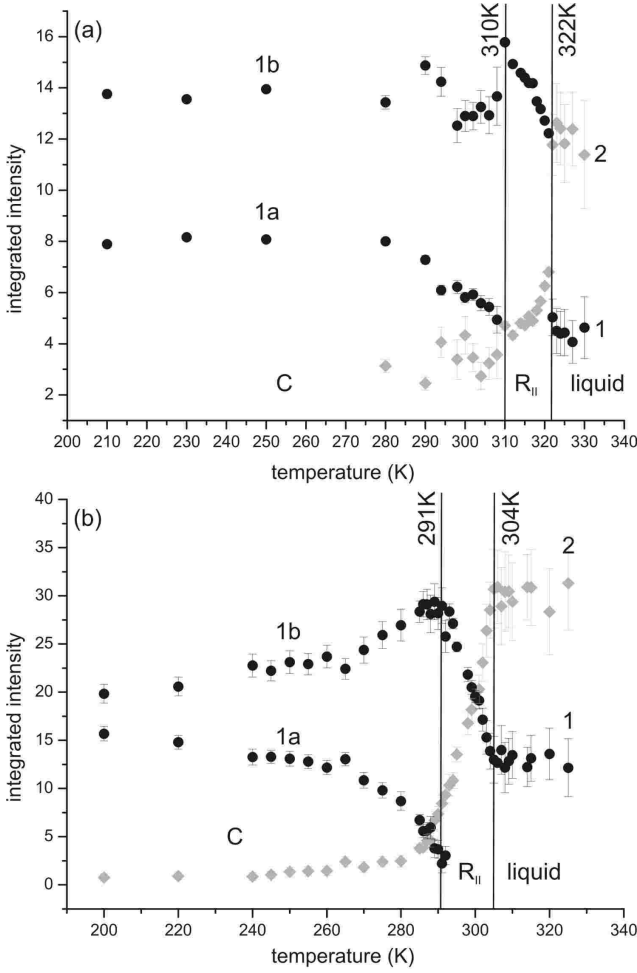


FIG. 12: Integrated intensity of the CH - scissor peak vs temperature for (a) bulk $C_{16}H_{33}OH$ and (b) confined $C_{16}H_{33}OH$ (the peak labels refer to Fig. 10).

form, that is characteristic for confined $C_{16}H_{33}OH$ (a quantitative analysis of bulk $C_{16}H_{33}OH$ is difficult due to the superposition of β - and γ -form). Assuming that the inner force constant f_α does not change at the phase transition, the intermolecular force constants $f_{3,j}$ can be evaluated from the observed splitting of the scissor band as described in Appendix B (see Eq. (30)). The values needed are the lattice parameters (see Table I) and the herringbone angle ζ between the projection of the backbone and the a -axis (see Fig. 14). The latter one is determined via Eq. (29) and the measured intensities of the two CH_2 -scissoring-peaks. For confined $C_{16}H_{33}OH$ we have $I_a = 13.29$ and $I_b = 22.23$ yielding an angle of $\zeta = 37.7^\circ$ (see Fig. 12b for $T = 245$ K). We display the intermolecular force constants in Table IV. For comparison, we also list literature values for an alkane, $C_{23}H_{48}$ at 90 K, which have been evaluated in the same way⁴⁰. This alkane and $C_{16}H_{33}OH$ exhibit a similar structure: The backbones of the molecules consist of the same CH_2 -units and both take the β -form at low-temperatures. In addition, also the values of the lattice constants for

	bulk		confinement	
	liquid	R_{II}	liquid	R_{II}
scissor [cm^{-1}]	1467	1467	1467	1467
sym. stretch [cm^{-1}]	2854	2851	2854	2851
assym. stretch [cm^{-1}]	2927	2921	2924	2918
f_d [N/m]	455	453	454	452
f_α [N/m]	56 ± 1	56 ± 1	57 ± 1	57 ± 1

TABLE III: Wavenumbers $\bar{\nu} = \omega/(2\pi c)$ (with ω being the angular frequency and c the speed of light) and resulting stretching and bending force constants in the liquid and R_{II} phase of bulk and confined $C_{16}H_{33}OH$. f_α has been evaluated using both the Eq. (27) and the Eq. (28). The difference yields the specified uncertainty. f_α are in units of N/m (see Eq. (5) in Appendix A and Ref.⁴¹). To get f_α in units Nm/rad^2 one has to multiply f_α with d^2 , where $d = 1.09 \cdot 10^{-10}$ m is the CH bond length.

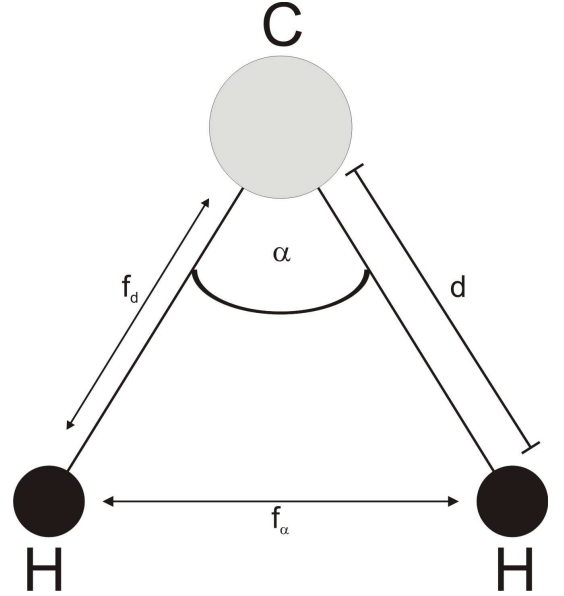


FIG. 13: CH_2 molecules with C-H bondlength d , H-C-H angle α and the resulting inner force constants f_d and f_α

$C_{23}H_{48}$, $a = 7.45$ Å and $b = 4.96$ Å, are close to those of $C_{16}H_{33}OH$ (see Tab. I). Due to this structural similarity the intermolecular distances listed in Table IV are similar, however, the respective force constants differ slightly by 10 to 20%. This is mainly due to the orientation of CH_2 -groups (the projection of the backbones on the a - b -plane) characterized by the herringbone angle ζ . For $C_{16}H_{33}OH$ $\zeta = 37.7^\circ$ holds, for the alkane $\zeta = 42^\circ$.

This difference is probably due to the presence of polar OH-groups in $C_{16}H_{33}OH$ that are strongly interacting and thus have an impact on the molecular orientation. The above comparison confirms once again that confined $C_{16}H_{33}OH$ takes the β -form in contrast to the bulk material (γ - and β -form).

In order to assess the validity of our analysis, we

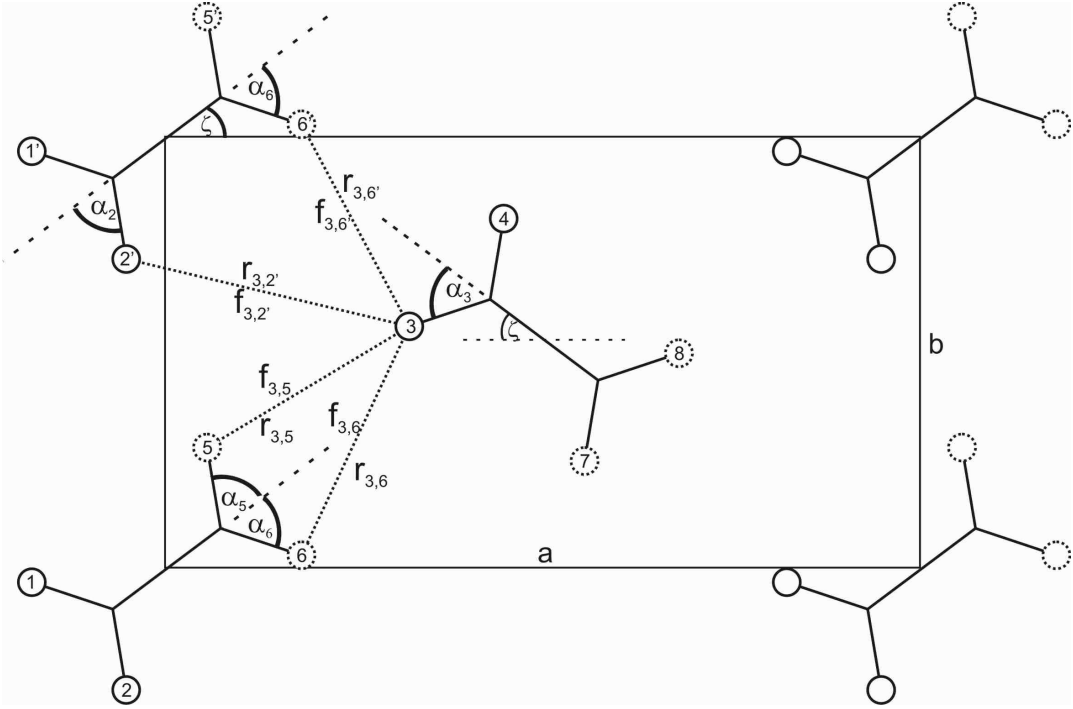


FIG. 14: Lattice of $C_{16}H_{33}OH$ in the C phase of the β -form, i. e. a view on the a-b-plane perpendicular to the molecules axis (compare with Fig. 3). Solid circles are H-atoms in the same plane, dashed circles are H-atoms lying in a plane above.

also calculate the theoretical band splitting of the CH_2 -scissoring vibration and compare it with the measured values. Using the values from Table IV as well as Eqs. (33) and (34), we get a theoretical value of $\Delta\overline{\nu}_{calc} = 8.1 \text{ cm}^{-1}$ for confined $C_{16}H_{33}OH$ at $T = 245 \text{ K}$. The measured band splitting is $\Delta\overline{\nu}_{meas} = 7.8 \text{ cm}^{-1}$. Therefore, the experimental data is in good agreement with the theory.

IV. SUMMARY

We have studied the structure and molecular dynamics of n-hexadecanol confined in nanochannels of mesoporous silicon and of bulk n-hexadecanol in their respective phases (in the order of decreasing temperature: liquid, rotator R_{II} and C). For this purpose we have performed x-ray and infrared-measurements.

The transition-temperatures for confined $C_{16}H_{33}OH$ are lower than for bulk $C_{16}H_{33}OH$ ($\Delta T \simeq 20 \text{ K}$, see Table II). In addition, under confinement the phase transitions are smeared, probably due to a distribution of pore diameters. Geometrical confinement does not affect the innermolecular force constants of the CH_2 -scissoring vibration (see Table III) but has an impact on the molecular arrangement. The R_{II} phase of both bulk and confined hexadecanol is characterized by an orthorhombic subcell, where the chain axis are parallel to the layer normal (see Fig. 4). However, in the low-temperature C phase there is a fundamental structural difference. While bulk $C_{16}H_{33}OH$ exhibits a polycrystalline mixture of β - and γ -forms (see Figs. 2 and 3), geometrical confinement favors a phase closely related to the β -form: only crystallites with an orthorhombic subcell are formed, where the chain axes are parallel to the bi-layer normal. However, the γ -form having a monoclinic subcell, in which the chain axis are tilted with respect to the layer normal, is suppressed. A reason for this might be the irregular shape of the nanochannels, into which the crystallites have to fit, favoring the formation of the geometrically

H-Atoms	force constant	confined $C_{16}H_{33}OH$ (this work) $\zeta = 37.7^\circ$		bulk $C_{23}H_{48}$ (Ref. ⁴⁰) $\zeta = 42^\circ$	
		distances (Å)	10^{-21} Nm	distances (Å)	10^{-21} Nm
3-2'	$f_{3,2'}$	2.85	-4.674	2.79	-5.837
3-5	$f_{3,5}$	2.59	-2.775	2.70	-2.376
3-6	$f_{3,6}$	2.96	-3.508	2.94	-3.920
3-6'	$f_{3,6'}$	2.96	-3.508	2.94	-3.920

TABLE IV: Distances between two neighboring hydrogen atoms and the resulting interaction force constants in the C phase confined $C_{16}H_{33}OH$ (β -form). ζ denotes the herringbone angle between the projection of the backbone and the a-axis (see Fig. 14). For comparison, we also list literature values for an alkane, $C_{23}H_{48}$ at 90 K, that also takes the β -form⁴⁰. The CH_2 -backbones of both molecules are similar, but $C_{16}H_{33}OH$ exhibits an additional polar OH-group that affects the orientation angle ζ .

more simple and less bulky form^{3,39} (see Fig. 6). Since only the pure β -form is present under confinement, we were able to evaluate the inter-molecular force constants of the CH₂-scissor vibration. Also the orientation of the

β -crystallites has been determined: the molecules are arranged with their long axis perpendicular to the pore axis.

- ¹ L. D. Gelb, K. E. Gubbins, R. Radhakrishnan and M. Sliwinska-Bartkowiak, Rep. Prog. Phys. **62** (1999) 1573.
- ² C. Alba-Simionesco, B. Coasne, G. Dosseh, G. Dudziak, K.E. Gubbins, R. Radhakrishnan and M.G. Sliwinska-Bartkowiak, J. Phys. Condens. Mat. **18**, R15 (2006).
- ³ H. K. Christenson, J. Phys. Condens. Mat. **13**, R95 (2001).
- ⁴ K. Knorr, P. Huber and D. Wallacher, Z. Phys. Chem. **222**, 257 (2008).
- ⁵ J. Koppensteiner, W. Schranz and M. R. Puica, Phys. Rev. B **78**, 054203 (2008).
- ⁶ P. Scheidler, W. Kob and K. Binder, Europhys. Lett. **52**, 277 (2000).
- ⁷ F. Kremer, A. Huwe, M. Arndt, P. Behrens and W. Schwieger, J. Phys. Condens. Matter **11** A175 (1999).
- ⁸ C. L. Jackson and G. B. McKenna, J. Non-Cryst. Solids **131-133**, 221 (1991).
- ⁹ G. Barut, P. Pissis, R. Pelster and G. Nimtz, Phys. Rev. Lett. **80**, 3543 (1998).
- ¹⁰ R. Pelster, Phys. Rev. B **59**, 9214 (1999).
- ¹¹ D. Daoukaki, G. Barut, R. Pelster, G. Nimtz, A. Kyritsis and P. Pissis, Phys. Rev. B **58** 5336 (1998).
- ¹² P. Pissis, A. Kyritsis, D. Daoukaki, G. Barut, R. Pelster and G. Nimtz, J. Phys. Condens. Matter **10**, 6205 (1998).
- ¹³ W. Schranz, M. R. Puica, J. Koppensteiner, H. Kabelka and A. V. Kityk, Europhys. Lett. **79**, 36003 (2007).
- ¹⁴ B. Frick, M. Koza and R. Zorn, Eur. Phys. J. E **12**, 3 (2003).
- ¹⁵ K. Knorr, D. Wallacher, P. Huber, V. Soprunyuk and R. Ackermann, Eur. Phys. J. E **12** 51 (2003).
- ¹⁶ D. Wallacher, R. Ackermann, P. Huber, M. Enderle and K. Knorr, Phys. Rev. B **64** 184203 (2001).
- ¹⁷ P. Huber, D. Wallacher, and K. Knorr, J. Low Temp. Phys. **111**, 419 (1998); P. Huber and K. Knorr, Phys. Rev. B **60**, 12657 (1999); ; P. Huber, D. Wallacher, K. Knorr, Phys. Rev. B **60**, 12666 (1999).
- ¹⁸ P. Huber, V. P. Soprunyuk and K. Knorr, Phys. Rev. E **74**, 031610 (2006).
- ¹⁹ A. Henschel, T. Hofmann, P. Huber and K. Knorr, Phys. Rev. E **75**, 021607 (2007).
- ²⁰ R. Montenegro and K. Landfester, Langmuir **19**, 5996 (2003).
- ²¹ B. Xie, G. Liu, S. Jiang, Y. Zhao and D. Wang, J. Phys. Chem. B **112**, 13310 (2008).
- ²² R. Valiullin and A. Khokhlov, Phys. Rev. E **73**, 051605 (2006).
- ²³ G. Crawford and S. Zumer (Editors), Liquid Crystals in Complex Geometries (Taylor and Francis, London, 1996).
- ²⁴ A. V. Kityk, M. Wolff, K. Knorr, D. Morineau, R. Lefort and P. Huber, Phys. Rev. Lett. **101**, 187801 (2008).
- ²⁵ P. Huber, D. Wallacher and J. Albers, K. Knorr, Europhys. Lett. **65**, 351 (2004).
- ²⁶ V. Lehmann, U. Gösele, Appl. Phys. Lett. **58**, 856 (1991); V. Lehmann, R. Stengl and A. Luigart, Materials Science and Engineering B **69-70**, 11 (2000);
- ²⁷ X. G. Zhang, J. Electrochem. Soc. **151**, C69 (2004);
- ²⁸ A. G. Cullis, L. T. Canham and P. D. J. Calcott, J. Appl. Phys. **82**, 909 (1997).
- ²⁹ S. Gruener and P. Huber, Phys. Rev. Lett. **100**, 064502 (2008).
- ³⁰ P. Huber, S. Gruener, C. Schaefer, K. Knorr and A. V. Kityk, Eur. J. Phys. Special Topics **141** 101 (2007).
- ³¹ V. Métivaud, A. Lefèvre, L. Ventolà, P. Négrier, E. Moreno, T. Calvet, D. Mondieig and M.A. Cuevas-Diarte, Chem. Mater. **17**, 3302 (2005).
- ³² S. Abrahamsson, G. Larsson and E. von Sydow, Acta Cryst. **13**, 770 (1960).
- ³³ M. Tasumi, T. Shimanouchi, A. Watanabe and R. Goto, Spectrochim. Acta **20**, 629 (1964).
- ³⁴ L. Ventolà, M. Ramirez, T. Calvet, X. Solans, M.A. Cuevas-Diarte, P. Négrier, D. Mondieig, J.C. van Miltenburg, H.A.J. Oonk, Chem. Mater. **14**, 508 (2002).
- ³⁵ E. B. Sirota and X. Z. Wu, J. Chem. Phys. **105**, 7763 (1996).
- ³⁶ A. Henschel, P. Huber and K. Knorr, Phys. Rev. E **77**, 042602 (2008).
- ³⁷ M. Steinhart, P. Göring, H. Dernaika, M. Prabhakaran, U. Gösele, E. Hempel and T. Thurn-Albrecht, Phys. Rev. Lett. **97**, 027801 (2006).
- ³⁸ P. A. Palibin and A. I. Froiman, Z. Kristallogr. **85**, 322 (1933); P. W. Bridgman, Proc. Amer. Acad. Arts Sci. **60** 305 (1925).
- ³⁹ K. Morishige and K. Kawano, J. Chem. Phys. **112**, 11023 (2000).
- ⁴⁰ R. G. Snyder, J. Mol. Spectroscopy **7**, 116 (1961).
- ⁴¹ A. G. Meister and F. F. Cleveland, Am. J. Physics **14**, 13 (1946).
- ⁴² E. B. Wilson Jr., J. Chem. Physics **7**, 1047 (1939).
- ⁴³ H. Siebert, Anwendungen der Schwingungsspektroskopie in der anorganischen Chemie, Springer-Verlag, Berlin (1966).
- ⁴⁴ M. Tasumi, T. Shimanouchi, J. Chem. Phys. **43**, 1245 (1965).
- ⁴⁵ R. S. Stein, J. Chem. Phys. **23**, 734 (1955).
- ⁴⁶ D. A. Dows, J. Chem. Phys. **32**, 1342 (1960).
- ⁴⁷ J. deBoer, Physica **9**, 363 (1942).

Appendix A

In this section we show how the innermolecular force constants of the CH₂-groups can be evaluated using three characteristic vibration frequencies, that are easily measured: the scissor vibration as well as the symmetric and asymmetric CH-bond stretching. For this purpose we apply the Wilson FG - matrix method⁴². We use the notation of Meister and Cleveland for the similar H₂O molecule⁴¹ and perform the calculations in the same way.

Fig. 13 shows a single CH₂ - molecule. In the following we will neglect the influence of the neighboring molecules on this one. $d = 1.09$ Å is the length of the C - H bond and $\alpha = 109.47^\circ$ the angle between the two C - H bonds³². This kind of molecule belongs to the C_{2v} point group. This means, there are two vibrations of type A_1 (symmetric stretching and bending vibration) and one vibration of type B_2 (asymmetric stretching vibration). The internal coordinates of this molecule are Δd_1 , Δd_2 and $\Delta\alpha$. Δd_1 and Δd_2 mean changes in the bond length of the two C - H - bonds and $\Delta\alpha$ changes in the angle between the two bonds. Therefore we get three symmetry coordinates, two for A_1 and one for B_2 . If we assume d being the equilibrium C - H bond length, then we obtain for the three symmetry coordinates:

$$R_1 = \sqrt{\frac{1}{2}}\Delta d_1 + \sqrt{\frac{1}{2}}\Delta d_2 \quad (1)$$

$$R_2 = \Delta\alpha \cdot d \quad (2)$$

$$R_3 = \sqrt{\frac{1}{2}}\Delta d_1 - \sqrt{\frac{1}{2}}\Delta d_2 \quad (3)$$

Now, we have to calculate the \mathbf{F} matrix, related to the potential energy, and the \mathbf{G} matrix related to the kinetic energy. The potential energy can be written as

$$2V = \sum f_{ik}r_i r_k \quad (4)$$

and with the internal coordinates

$$2V = f_d \left[(\Delta d_1)^2 + (\Delta d_2)^2 \right] + f_\alpha (d\Delta\alpha)^2 + 2f_{d\alpha} (\Delta d_1 + \Delta d_2) (d\Delta\alpha) + 2f_{dd} (\Delta d_1) (\Delta d_2) \quad (5)$$

Now we set $d_1 = d_2 = d$ and write Eq. (5) as

$$2V = \sum F_{jl} R_j R_l \quad (6)$$

with $F_{jl} = F_{lj}$. In matrix form, Eqs. (4) and (5) become

$$2V = \mathbf{r}' \mathbf{f} \mathbf{r} \quad (7)$$

and

$$2V = \mathbf{R}' \mathbf{F} \mathbf{R} \quad (8)$$

\mathbf{r}' and \mathbf{R}' are the transposes of \mathbf{r} and \mathbf{R} . With Eqs. (7) + (8)

$$\mathbf{r}' \mathbf{f} \mathbf{r} = \mathbf{R}' \mathbf{F} \mathbf{R} \quad (9)$$

The R_i 's are linear combinations of the r_i 's

$$R_i = \sum_k U_{ik} r_k \quad (10)$$

$$\mathbf{R} = \mathbf{U} \mathbf{r}$$

Since the R_i 's are orthogonal and normalized, then $\mathbf{U}^{-1} = \mathbf{U}'$ and

$$\mathbf{r} = \mathbf{U}' \mathbf{R} \quad (11)$$

$$\mathbf{r}' = (\mathbf{U}' \mathbf{R})' = \mathbf{R}' \mathbf{U} \quad (12)$$

This means with Eqn. (10)

$$\mathbf{R}' (\mathbf{U} \mathbf{f} \mathbf{U}') \mathbf{R} = \mathbf{R}' \mathbf{F} \mathbf{R} \quad (13)$$

$$\mathbf{F} = \mathbf{U} \mathbf{f} \mathbf{U}' \quad (14)$$

The \mathbf{F} matrix is

	Δd_1	Δd_2	$\Delta\alpha$
Δd_1	f_d	f_{dd}	$df_{d\alpha}$
Δd_2	f_{dd}	f_d	$df_{d\alpha}$
$\Delta\alpha$	$df_{d\alpha}$	$df_{d\alpha}$	$d^2 f_\alpha$

The \mathbf{U} matrix for type A_1 is

A_1	Δd_1	Δd_2	$\Delta\alpha$
R_1	$\sqrt{\frac{1}{2}}$	$\sqrt{\frac{1}{2}}$	0
R_2	0	0	1

and for B_2

B_2	Δd_1	Δd_2	$\Delta\alpha$
R_3	$\sqrt{\frac{1}{2}}$	$-\sqrt{\frac{1}{2}}$	0

So, for the type A_1 the \mathbf{F} matrix is

$$\mathbf{F}_{A_1} = \mathbf{U} \mathbf{f} \mathbf{U}' = \begin{pmatrix} F_{11} & F_{12} \\ F_{21} & F_{22} \end{pmatrix} = \begin{pmatrix} f_d + f_{dd} & \sqrt{2} df_\alpha \\ \sqrt{2} df_\alpha & d^2 f_\alpha \end{pmatrix} \quad (15)$$

and for the B_2 type

$$\mathbf{F}_{B_2} = (F_{33}) = (f_d - f_{dd}) \quad (16)$$

The exact derivation of the \mathbf{G} matrix shouldn't be shown here. It can be gleaned by Meister and Cleveland⁴¹. Only the most important steps shall be explained here.

If only non-degenerate vibrations are present, the elements of the kinetic energy matrix can be written as

$$G_{jl} = \sum_p \mu_p g_p \mathbf{S}_j^{(t)} \mathbf{S}_l^{(t)} \quad (17)$$

where j and l refer to symmetry coordinates used in determining the \mathbf{S} vector, p refer to a set of equivalent atoms, a typical one of the set being t . μ_p is the reciprocal of the mass of the typical atom t_p and g_p is the number of equivalent atoms in the p th set. The \mathbf{S} vector is given by

$$\mathbf{S}_j^{(t)} = \sum_k U_{jk} s_{kt} \quad (18)$$

where j , U_{jk} and \sum_k have the same meaning as above. s_{kt} can be expressed in terms of unit vectors along the chemical bonds and depends on the changes in the bond length or the angle between the bonds. So, the \mathbf{G} matrix for the A_1 vibration type has the form

$$\mathbf{G}_{A_1} = \begin{pmatrix} G_{11} & G_{12} \\ G_{21} & G_{22} \end{pmatrix} = \begin{pmatrix} \mu_H + \mu_C(1 + \cos \alpha) & -\frac{\mu_C \sqrt{(2)} \sin \alpha}{d} \\ -\frac{\mu_C \sqrt{(2)} \sin \alpha}{d} & \frac{2\mu_H + \mu_C(1 - \cos \alpha)}{d} \end{pmatrix} \quad (19)$$

and for the B_2 vibration type

$$\mathbf{G}_{B_2}(G_{33}) = (\mu_H + \mu_C(1 - \cos \alpha)) \quad (20)$$

To determine the frequencies, one has to solve the equation

$$|\mathbf{GF} - \lambda \mathbf{E}| = 0 \quad (21)$$

where $\lambda = \omega^2 = (\overline{\nu} 2\pi c)^2$ denotes the square of the angular frequency. For the A_1 type one gets the equation

$$\lambda^2 - \lambda(F_{11}G_{11} + 2F_{12}G_{12} + F_{22}G_{22}) + \begin{vmatrix} F_{11} & F_{12} \\ F_{21} & F_{22} \end{vmatrix} \cdot \begin{vmatrix} G_{11} & G_{12} \\ G_{21} & G_{22} \end{vmatrix} = 0 \quad (22)$$

and for the B_2 type

$$\lambda_3 - F_{33}G_{33} = 0 \quad (23)$$

Eq. (22) can be separated with the Vieta expression⁴³. Inserting the terms for the F_{ij} and G_{ij} , we obtain

$$\begin{aligned} \lambda_1 + \lambda_2 &= (f_d + f_{dd})[\mu_C(1 + \cos \alpha) + \mu_H] \\ &\quad + 2f_\alpha[\mu_C(1 - \cos \alpha) + \mu_H] - 4f_{d\alpha}\mu_C \sin \alpha \quad (24) \\ \lambda_1 \cdot \lambda_2 &= [(f_d + f_{dd})f_\alpha - 2f_{d\alpha}^2]2\mu_H(2\mu_C + \mu_H) \end{aligned}$$

For Eq. (23) one obtains

$$\lambda_3 = (f_d - f_{dd})[\mu_C(1 - \cos \alpha) + \mu_H] \quad (25)$$

Neglecting the coupling constants f_{dd} and $f_{d\alpha}$ allows to evaluate the innermolecular force constants using the measured wave numbers, $\overline{\nu}_{d,sym} = \sqrt{\lambda_1}/(2\pi c)$, $\overline{\nu}_\alpha = \sqrt{\lambda_2}/(2\pi c)$ and $\overline{\nu}_{d,asym} = \sqrt{\lambda_3}/(2\pi c)$. Then Eq. (25) yields

$$f_d = (2\pi c)^2 \cdot \frac{\overline{\nu}_{d,asym}^2}{\mu_C(1 - \cos \alpha) + \mu_H} \quad (26)$$

Inserting this result into Eq. (24) yields

$$f_\alpha = (2\pi c)^2 \cdot \frac{\overline{\nu}_{d,sym}^2 \cdot \overline{\nu}_\alpha^2}{\overline{\nu}_{d,asym}^2} \cdot \frac{\mu_C(1 - \cos \alpha) + \mu_H}{2\mu_H(2\mu_C + \mu_H)} \quad (27)$$

There is a second possibility to evaluate f_α , i. e. by inserting Eq. (26) into Eq. (24). This yields

$$f_\alpha = (2\pi c)^2 \cdot \frac{\overline{\nu}_{d,sym}^2 + \overline{\nu}_\alpha^2 - \overline{\nu}_{d,asym}^2}{2(\mu_C(1 - \cos \alpha) + \mu_H)} \cdot \frac{\mu_C(1 + \cos \alpha) + \mu_H}{\mu_C(1 - \cos \alpha) + \mu_H} \quad (28)$$

Taking the measured wavenumbers listed in Table III and the average angle between the CH-bonds, $\alpha = 109.4^\circ$, as well as the masses of the atoms, $1/\mu_C = 12u$ and $1/\mu_H = 1u$ ($u = 1.6606 \cdot 10^{-27}$ kg), Eqs. (26)-(28) yield the force constants listed in Table III. The difference in calculating f_α via Eq. (27) or Eq. (28) is below 3.1% confirming that the inner-molecular coupling terms can be neglected.

Appendix B

What follows is a summary of Snyder's derivation of the intermolecular force constants between the CH_2 groups of neighboring molecules that gives rise to a splitting of the scissor band at low temperatures⁴⁰. We show how this formalism can be applied to $\text{C}_{16}\text{H}_{33}\text{OH}$. An alternative description can be found in Ref.⁴⁴.

In Fig. 14 we display a hexagonal subcell of $\text{C}_{16}\text{H}_{33}\text{OH}$. While Stein⁴⁵ has taken only one pair of neighboring CH_2 into account to calculate the splitting of rocking and scissoring bands, Snyder has shown that more pairs have to be included. When we consider the distances of H-atoms from the H-atom no. 3 (see Fig. 14), then all atoms except no. 2', 6', 5 and 6 have distances larger than 3.7 Å. The internal coordinates α_i are always half of the angle between the C - H bonds of a CH_2 molecule. Solid circles are H-atoms in the same plane, dashed circles H-atoms in a plane above or below.

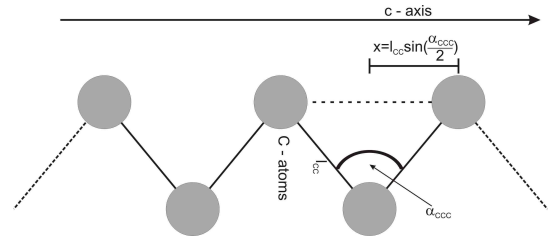


FIG. 15: Lateral view at the long axis of the $\text{C}_{16}\text{H}_{33}\text{OH}$ chain, x is the projection of the C - C distance on the c -axis of the crystal lattice

Now, we want to write the positions of these five H-atoms as a vector. Fig. 15 shows the lateral view of a part of the $\text{C}_{16}\text{H}_{33}\text{OH}$ chain. With values from Abrahamsson³² for $l_{CC} = 1.545$ Å and $\alpha_{CCC} = 110.4^\circ$, we can calculate

the distance of the a-b-plane to the corresponding plane above or below with

$$x = l_{CC} \sin\left(\frac{\alpha_{CCC}}{2}\right) = 1.2687 \text{ \AA}$$

Assuming that the hydrogen in the central plane has the c component 0, the hydrogen in the plane above has the component $c = 1.2687 \text{ \AA}$.

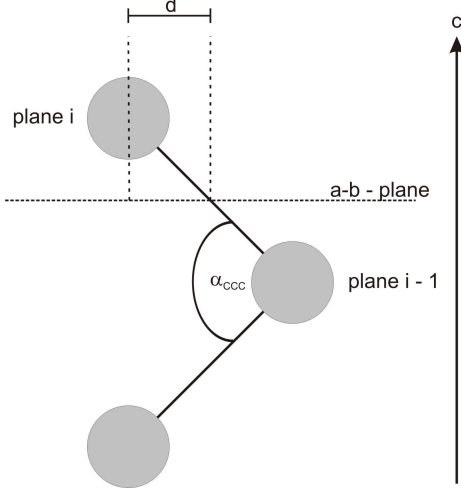


FIG. 16: Lateral view at the long axis of the $C_{16}H_{33}OH$ chain, d is the projection of half of the C - C distance on the a-b-plane of the subcell.

The projection of the C - C bond in the a-b-plane is according to Fig. 16

$$d = \frac{l_{CC}}{2} \cos\left(\frac{\alpha_{CCC}}{2}\right) = 0.4409 \text{ \AA}$$

Taking the point **0** for the lower left edge of the ab - plane the five atoms have the coordinates:

$$\begin{aligned} H_3 &= \begin{pmatrix} \frac{a}{2} - d \cos(\zeta) - l \cos(\alpha_3 - \zeta) \\ \frac{b}{2} + d \sin(\zeta) - l \sin(\alpha_3 - \zeta) \\ 0 \end{pmatrix} \\ H_{2'} &= \begin{pmatrix} -d \cos(\zeta) + l \sin(\alpha_{2'} - \frac{\pi}{2} + \zeta) \\ b - d \sin(\zeta) - l \cos(\alpha_{2'} - \frac{\pi}{2} + \zeta) \\ 0 \end{pmatrix} \\ H_5 &= \begin{pmatrix} d \cos(\zeta) - l \sin(\alpha_5 - \frac{\pi}{2} + \zeta) \\ d \sin(\zeta) + l \cos(\alpha_5 - \frac{\pi}{2} + \zeta) \\ 1.2674 \end{pmatrix} \\ H_6 &= \begin{pmatrix} d \cos(\zeta) + l \cos(\alpha_6 - \zeta) \\ d \sin(\zeta) - l \sin(\alpha_6 - \zeta) \\ 1.2674 \end{pmatrix} \\ H_{6'} &= \begin{pmatrix} d \cos(\zeta) + l \cos(\alpha_{6'} - \zeta) \\ b + d \sin(\zeta) - l \cos(\alpha_{6'} - \zeta) \\ 1.2674 \end{pmatrix} \end{aligned}$$

with a and b being the lattice constants of the crystalline phase. We get the distances between the atom 3 and the other ones (see Fig. 14) with

$$r_{3j} = |H_3 - H_j| \quad (28)$$

where $j = 2', 6', 5, 6$ is. The herringbone angle ζ (see the upper left corner of Fig. 14) can be determined with the relation⁴⁰

$$\frac{I_a}{I_b} = \tan^2 \zeta \quad (29)$$

where I_a is the integrated intensity of the scissoring mode, which is polarized in the a direction (higher mode at 1473 cm^{-1}) and I_b the one of the mode, which is polarized in the b direction (lower mode at 1462 cm^{-1}).

With the distances of two hydrogen atoms H_3 and H_j ($=r_{3,j}$) [in our case 3 denotes the central H-atom (see Fig. 14) and $j = 2', 5, 6, 6'$ the neighboring H-atoms that interact] we obtain the intermolecular force constants $f_{3,j}$:

$$\begin{aligned} f_{3,j} &= \frac{\partial^2 V_{HH}}{\partial \alpha_3 \partial \alpha_j} \\ &= \left(\frac{\partial^2 V_{HH}}{\partial r^2} \right)_{r_{3j}} \left(\frac{\partial r}{\partial \alpha_3} \right) \left(\frac{\partial r}{\partial \alpha_j} \right) \end{aligned} \quad (30)$$

where V_{HH} is the hydrogen repulsion potential introduced by Dows⁴⁶:

$$V_{HH} = 1.2 \cdot 10^{-10} e^{-3.52r} \quad (31)$$

with r in \AA .

The values of $(\partial^2 V_{HH} / \partial r^2)_{r_{ij}}$ are obtained from Eq. (32).

$$\beta = \frac{\partial^2 V_{HH}}{\partial r^2} = 1.486848 \cdot 10^{-9} e^{-3.52r} \quad (32)$$

with β in $\frac{\text{ergs}}{\text{\AA}^2} = 10^{16} \frac{\text{dyne}}{\text{cm}} = 10^{13} \frac{\text{N}}{\text{m}}$.

The measured intensity ratio (Eq. (29)) allows us to calculate the distances r_{ij} as well as the partial derivatives $\partial r / \partial \alpha_i$ (see Eq. (28) and above). Finally, by knowing the intermolecular force constants $f_{3,j}$ from Eq. (32) we can evaluate the band splitting of the scissoring vibration⁴⁰. For the angular frequencies

$$\bar{\nu}_1^2 - \bar{\nu}_2^2 = \left(\frac{1}{2\pi c} \right)^2 \cdot \underbrace{G_a^B \cdot \{2f_{3,2'} - 2(f_{3,6} + f_{3,6'}) - 4f_{3,5}\}}_{\Delta \lambda^B} \quad (33)$$

holds³ with

³ In Snyder's general theory the force constants for the scissoring vibration are denominated as f_a^3 ($= f_{3,2'}$), f_b^2 ($= f_{3,6} + f_{3,6'}$) and f_b^3 ($= f_{3,5}$).

$$G_a^B = \frac{4}{3}Q_R^2\mu_C + Q_r^2\mu_H \quad (34)$$

Here $1/\mu_C = 12u$ and $1/\mu_H = 1u$ denote the masses of the atoms ($u = 1.6606 \cdot 10^{-27}$ kg), $1/Q_R = 1.545 \cdot 10^{-10}$ m the C-C distance and $1/Q_r = 1.09 \cdot 10^{-10}$ m the C-H distance, so that $G_a^B = (0.88825/u) \text{ \AA}^{-2} = 5.349 \cdot 10^{46} (\text{N m})^{-1} \text{s}^{-2}$. For the band splitting of the wavenumbers we thus obtain

$$\begin{aligned} \Delta\bar{\nu} &= \bar{\nu}_1 - \bar{\nu}_2 \\ &= \left(\frac{1}{2\pi c} \right)^2 \cdot \frac{G_a^B \cdot \{2f_{3,2'} - 2(f_{3,6} + f_{3,6'}) - 4f_{3,5}\}}{\bar{\nu}_1 + \bar{\nu}_2} \end{aligned} \quad (35)$$

Inserting the values of Table IV, i. e. $(2f_{3,2'} - 2(f_{3,6} + f_{3,6'}) - 4f_{3,5}) = 15.784 \cdot 10^{-21}$ Nm for confined $\text{C}_{16}\text{H}_{33}\text{OH}$, as well as the respective wave numbers, that we take from Fig. 11 at low temperatures (labels 1a and 1b: $\bar{\nu}_1 + \bar{\nu}_2 \simeq 2 \cdot 146700 \text{ 1/m}$) we get $\Delta\bar{\nu} = 810 \text{ m}^{-1} \equiv 8.1 \text{ cm}^{-1}$ for confined $\text{C}_{16}\text{H}_{33}\text{OH}$.